



HAL
open science

On The Efficiency of P -Wave Coda Autocorrelation in Recovering Crustal Structure: Examples From Dense Arrays in the Eastern United States

Chuang Wang, Benoit Tauzin, Thanh-son Pham, Hrvoje Tkalčić

► **To cite this version:**

Chuang Wang, Benoit Tauzin, Thanh-son Pham, Hrvoje Tkalčić. On The Efficiency of P -Wave Coda Autocorrelation in Recovering Crustal Structure: Examples From Dense Arrays in the Eastern United States. *Journal of Geophysical Research : Solid Earth*, 2020, 125 (12), 10.1029/2020JB020270 . hal-03025231

HAL Id: hal-03025231

<https://hal.science/hal-03025231v1>

Submitted on 7 Dec 2020

HAL is a multi-disciplinary open access archive for the deposit and dissemination of scientific research documents, whether they are published or not. The documents may come from teaching and research institutions in France or abroad, or from public or private research centers.

L'archive ouverte pluridisciplinaire **HAL**, est destinée au dépôt et à la diffusion de documents scientifiques de niveau recherche, publiés ou non, émanant des établissements d'enseignement et de recherche français ou étrangers, des laboratoires publics ou privés.



1 **On the efficiency of P-wave coda autocorrelation in**
2 **recovering crustal structure: examples from dense**
3 **arrays in the eastern US**

4 **Chuang Wang¹, Benoît Tauzin^{1,2}, Thanh-Son Pham¹, and Hrvoje Tkalčić¹**

5 ¹Research School of Earth Sciences, The Australian National University, Canberra, ACT 2601, Australia.

6 ²Université de Lyon, Université Claude Bernard Lyon 1, ENS, CNRS, Laboratoire de Géologie de Lyon :
7 Terre, Planètes, Environnement, 69622 Villeurbanne, France.

8 **Key Points:**

- 9 • We investigate the efficiency of P-wave coda autocorrelation in recovering crustal
10 architecture
11 • We compare imaging from P-wave coda vertical autocorrelations and radial re-
12 ceiver functions using dense profiles from US arrays
13 • Vertical autocorrelations clearly outperform radial receiver functions in presence
14 of a sedimentary basin

Corresponding author: Benoit Tauzin, benoit.tauzin@univ-lyon1.fr

-1-

This article has been accepted for publication and undergone full peer review but has not been through the copyediting, typesetting, pagination and proofreading process which may lead to differences between this version and the Version of Record. Please cite this article as doi: 10.1029/2020JB020270

Abstract

Due to a sharp contrast in elastic properties across the basement rocks of sedimentary basins (SBs), strong reverberations are generated during the passage of seismic waves. Traditional receiver function methods become inadequate for imaging crustal structure due to the existence of these strong reverberations. We investigate the feasibility of an auto-correlation technique to extract vertical component receiver functions from teleseismic earthquake data and the efficiency of the method to image the crustal architecture in presence of a SB. The method involves spectral whitening followed by autocorrelation, and stacking in the depth domain. We show promising results when using temporary seismic networks in the eastern US. Using synthetic and field-data examples, we demonstrate that autocorrelations are more efficient than classical radial receiver functions in recovering structural properties in a SB context. We also perform a joint analysis of the amplitudes on radial and vertical receiver functions for characterizing the thickness of the Mohorovičić discontinuity (Moho). We find that the Moho in the eastern US is a transitional layer (up to 5 km thick) instead of a sharp boundary. Further, we point out that it is challenging to unambiguously pick and interpret reflected phases on autocorrelations because of the effects of reverberations, cross-mode contaminations, and a narrow frequency band limiting the resolution of velocity gradients. We believe that this is not a unique problem to our particular dataset, but to most studies based on autocorrelations, and we therefore send a message of caution for future interpretations based on this technique.

1 Introduction

Teleseismic earthquakes occur at distances of more than thousands of kilometers away from the recorders (typically epicentral distances larger than 30°). At these epicentral distances, the incoming teleseismic wave is approximately a plane wave with a relatively steep incidence angle. Burdick and Helmberger (1974) noticed that vertically polarized teleseismic waveforms are dominated by the source, the near-source structure and the instrument effects. The near-receiver structure, due to a small incidence angle, influences mainly the compressional wave (P wave) response in the vertical seismograms. Similarly, the shear wave (S wave) response of the structure beneath a receiver can be retrieved from the horizontal seismograms. Langston (1979) proposed a technique to determine the near-receiver structural response by deconvolving the vertical component of teleseismic seismograms from the horizontal ones. Through deconvolution, the complicated source and wavefield propagation effects away from the receiver are removed from the horizontal components, and the results are referred to as the radial receiver functions (RFs). Vinnik (1977) introduced slightly earlier the correlation-based approach to compute receiver functions.

The introduction of auto- and cross-correlations to seismology predated the development of the RF method. The autocorrelation of the transmission response of an acoustic plane-wave was used by Claerbout (1968) to extract the reflection response of the stratification beneath a receiver. Autocorrelation is a mathematical operation that measures the similarity of a waveform with itself in a single time series. A similar operation, cross-correlation, involves two seismograms, and is used to build the radial RF with deconvolution (Clayton & Wiggins, 1976; Vinnik, 1977; Ammon, 1991). In the following, we will interchangeably use the terminology “autocorrelation” and “vertical RF”, because in practice the vertical RF can be built from the autocorrelation of the vertical component seismogram (Tauzin et al., 2019).

A few early studies used the principle of correlation for characterizing crustal structure (e.g., L. J. Burdick & Langston, 1977; X.-Q. Li & Nábělek, 1999; C. Langston & Hammer, 2001). In particular, C. Langston and Hammer (2001) suggested that all three components of the RFs should be involved in inferring Earth-structure models, and demon-

66 strated the reliability of the technique by means of using vertical-component P-wave (au-
67 tuncorrelation) RFs. More recent developments of the autocorrelation method make use
68 of the vertically propagating component of the seismic ambient noise (e.g., Tibuleac &
69 von Seggern, 2012; Gorbatov et al., 2013; Kennett, 2015; Kennett et al., 2015; Taylor et
70 al., 2016; Saygin et al., 2017; Becker & Knapmeyer-Endrun, 2018). The difference be-
71 tween the noise-based and event-based approaches is still under investigation (Kennett,
72 2015; Sun & Kennett, 2016; Romero & Schimmel, 2018; Buffoni et al., 2019; Tauzin et
73 al., 2019). The choice of filtering have been shown to play an important role in the re-
74 covery and type of recovered signal from noise autocorrelations (Helffrich, 2019) with two
75 main approaches. The first approach is inherited from standard radial RFs analysis and
76 makes use of frequencies smaller than 1 Hz (Tibuleac & von Seggern, 2012; Taylor et al.,
77 2016). This approach allows for the identification of individual reflected phases on au-
78 tuncorrelograms for subsequent picking and interpretation in terms of stratigraphy. The
79 second approach makes use of the high-frequency component of the noise that involves
80 an analysis within a narrow frequency band (Gorbatov et al., 2013; Kennett, 2015; Becker
81 & Knapmeyer-Endrun, 2018; Romero & Schimmel, 2018). In this second case, determin-
82 istic seismic arrivals are not anymore detected, and the interpretation is driven by changes
83 in the reflectivity patterns in autocorrelations.

84 In sedimentary basins (SBs), radial RFs are contaminated by a strong resonance
85 effect. As shown by e.g. Zheng et al. (2005), RFs from recording sites that are filled by
86 sediments are dominated by reverberations in the sedimentary layers within the first few
87 seconds after the direct P-arrival. Indeed, due to a strong, basal, impedance contrast,
88 the low-velocity sedimentary layer (LVZ) generates quite strong P-wave and S-wave re-
89 verberations and conversions. The superimposed reflections and conversion at the base
90 the sediments often dominate over the converted phases from deeper crustal disconti-
91 nities and mask corresponding information about Earth structure (Frederiksen & De-
92 laney, 2015). Thus, conventional methods based on the analyses of travel-times of con-
93 verted waves can lead to erroneous interpretations.

94 Several methods have been developed for mapping the crustal structure in SBs. Those
95 methods, designed to reduce SB reverberations, include downward continuation and wave-
96 field decomposition (Langston, 2011), autocorrelation with a resonance removal filter in
97 the frequency domain (Yu et al., 2015), and radial RF method to fit the waveforms and
98 invert for elastic structure of a SB (Piana Agostinetti et al., 2018). Wavefield downward
99 continuation method (Langston, 2011) requires a priori knowledge of Earth structure and
100 modeling to extract wave conversions. This method has been applied to estimate sed-
101 imentary and crustal structures (e.g., Tao et al., 2014). Another recent study investi-
102 gated sedimentary structure of basins in China from frequency dependent P-wave par-
103 ticle motion (Yang & Niu, 2019). Li et al. (2019) reported a joint inversion of Rayleigh
104 wave phase velocity, particle motion, and teleseismic body wave data for sedimentary
105 structures.

106 Here, we investigate the performance of a new method for imaging the crustal archi-
107 tecture based on the spectral whitening and autocorrelation of the vertical compo-
108 nent of teleseismic records (Pham & Tkalčić, 2017; Tauzin et al., 2019). We investigate
109 whether this method is appropriate for characterizing the crustal structure in presence
110 of a SB. Spectral whitening is the division in the frequency domain of the original spec-
111 trum by the running average of its amplitude. We show that this operation efficiently
112 filters out undesirable resonance associated with SBs. In comparison to the inversion of
113 radial RF waveforms, autocorrelation based on filtering is computationally efficient for
114 achieving direct imaging of the basin and crustal structure.

115 In order to demonstrate our method with dense seismic arrays, we analyze broad-
116 band data from temporary seismic arrays with quasi-linear geometry in the eastern US.
117 Recently, two studies have used the principle of correlation to analyze the crustal struc-
118 ture in the US. Delph et al. (2019) constrained the Moho depth and crustal V_p/V_s ra-

119 tio underneath 88 stations from the Transportable Array using vertical and radial com-
 120 ponent RFs. van IJsseldijk et al. (2019) used a dense seismic array in Minnesota and Wis-
 121 consin and a Global Phase Seismic Interferometry approach, which is based on autocor-
 122 relations of teleseismic P-waveforms, but recorded at small incidence angles.

123 The seismic arrays that we use for imaging the crust in eastern US run from the
 124 Quaternary deposits in the Mississippi embayment, through a region of thickened crust
 125 at the western border of the Appalachian, to Maine in the northeast. Our data are di-
 126 vided into three sub-arrays with various station density and operation time that sam-
 127 ple different geological settings. We investigate in particular the efficiency of the method
 128 for imaging a laterally variable crust overlaid in places by SBs. We present the general
 129 features of the processing. Given the amount of data and the processing for source equal-
 130 ization, a data selection procedure is implemented, which is dedicated to improving the
 131 signal-to-noise ratio of specific reflected arrivals. We observed coherent signals along the
 132 three sub-arrays. A comparison with a reference crustal model suggests that we are able
 133 to unambiguously image the Moho and the internal stratification of the crust, in con-
 134 trary to radial RFs that poorly perform in presence of a SB. We also find in the east-
 135 ern US the Moho to be a transitional layer (up to 5 km thick) instead of a sharp bound-
 136 ary.

137 2 Methods and Data

138 An example of vertical component RF for a simple one-layer crust is shown in Fig-
 139 ure 1b, with labels for major converted and reflected phases Ps , PPp , PPs and PSs .
 140 The paths are shown in Figure 1a. We also show in Figure 1b for comparison the theo-
 141 retical response recorded on the radial component. In our particular implementation
 142 of the vertical receiver function method, the extracted signal corresponds to the sequence
 143 of reflections (Figure 1b) in the stratification underneath the seismometer (Figure 1a).
 144 The main reflection being recorded on this vertical RF is the reflection from the top of
 145 the Moho discontinuity, $PPmp$, where "m" marks the Moho (Figure 1b). Its amplitude
 146 results from the interaction of the teleseismic wavefield with the free-surface, with a re-
 147 flection coefficient close to -1, and with the Moho interface, with a positive reflection co-
 148 efficient. The combined reflection response gives a negative amplitude for the Moho re-
 149 flection on the vertical RF record (Figure 1b). This response is not exactly the reflec-
 150 tion response as obtained within the frame of seismic interferometry (Claerbout, 1968;
 151 Wapenaar et al., 2010; Ruigrok & Wapenaar, 2012; Tauzin et al., 2019). Indeed, if we
 152 take the reflection response due to a virtual source located at the surface at the reflec-
 153 tion point of the teleseismic P-wave, then the negative reflection at the free surface is
 154 removed through the principle of interferometry, and the remaining reflection at the Moho
 155 is positive. Our estimated reflection response has therefore an opposite (negative) sign
 156 with respect to the P-wave reflection response in seismic interferometry imaging appli-
 157 cations.

We compute the vertical RFs using spectral whitening, followed by autocorrelation (Pham & Tkalčić, 2017; Tauzin et al., 2019). If $Z(f)$ is the spectrum of the vertical component, the vertical receiver function $E_z(f)$ is obtained from

$$E_z(f) \approx \frac{Z(f) Z^*(f)}{Z''(f)}, \quad (1)$$

where the superscript $*$ marks the complex conjugate and $Z(f) Z^*(f)$ is the autocorrelation written in the frequency domain. $Z''(f)$ is the regularized vertical component power spectrum taken as an approximation for the teleseismic source function. Each frequency sample is obtained through smoothing over a window of width W so the regularized vertical spectrum is

$$Z''(f) = \frac{1}{W} \int_{f-W/2}^{f+W/2} \|Z(\nu)\|^2 d\nu. \quad (2)$$

158 In the post-processing stage, we apply a 4th-order Butterworth filter with a band-
 159 pass chosen depending on the target structure. The frequency content necessary to im-
 160 age the shallow structure is higher (0.4 -1 Hz band-pass) than for imaging the Moho (0.2
 161 -1 Hz band-pass). We also use different values of the smoothing width W depending on
 162 the target interface (see Pham & Tkalčić, 2018). We discuss the choice of the W param-
 163 eter in section 5.3. We use a constant value of $W = 0.1$ Hz for targeting the Moho. We
 164 set W to a larger value, 0.4 Hz, when targeting the shallow stratification.

To improve the signal-to-noise ratio, all the vertical component RFs for a single
 station are stacked to build a high-quality reflection response. As the RFs are obtained
 over a large range of epicentral distances, the travel-time of P-wave reflected phases fol-
 lows a move-out due to the variable path-lengths of waves incoming on the stratification.
 For a single layer of thickness H and P-wave velocity v_p overlying a homogeneous half-
 space, the travel-time of the PPp mode with respect to direct P (Figure 1b) is expressed
 by

$$T_{PPp}(H, v_p, p) = 2H \sqrt{\frac{1}{v_p^2} - p^2}, \quad (3)$$

165 where p is the slowness of the impinging P-wave. We use the generalization of this ex-
 166 pression to horizontally stratified media to compute a time-to-depth relationship and con-
 167 vert the time-domain auto-correlations into the depth-domain (Tauzin et al., 2019). This
 168 relationship is mode-dependent, and leads to destructive interference of signals that do
 169 not follow the move-out of P-wave reflections PPp . Single station auto-correlations are
 170 then linearly stacked in the depth domain. Due to the fact that the PPms phase has a
 171 similar travel-time relation as PPmp, the PPms phase appears as a “second Moho” at
 172 deeper depth with weaker amplitude (see Z component in Figure 1b). We tested phase-
 173 weighted stacking (Schimmel & Paulssen, 1997) but did not find a major improvement
 174 in the quality of crustal images. We apply bootstrap resampling (Efron & Tibshirani,
 175 1991) for estimating the variability of stacked waveforms.

Despite the fact that equation (1) can be modified to extract radial receiver func-
 tions (Tauzin et al., 2019), we computed classical radial receiver functions through water-
 level deconvolution (Clayton & Wiggins, 1976). The difference resides in the (quasi-)absence
 of the PPp mode in water-level receiver functions (Tauzin et al., 2019). In that case, the
 radial RF is given by

$$E_r(f) \approx \frac{R(f) Z^*(f)}{Z'(f)}, \quad (4)$$

where $R(f)$ is the radial component spectrum. The regularized vertical spectrum $Z'(f)$
 is the initial spectrum that is leveled to a minimum amplitude defined by the water-level
 c (Clayton & Wiggins, 1976),

$$Z'(f) = \max(\|Z(f)\|^2, c \|Z\|_{\max}^2). \quad (5)$$

We apply in this case a Gaussian filter (Clayton & Wiggins, 1976; Ammon, 1991). The
 radial RFs are then depth-converted using a time-to-depth relationship for the direct Ps
 conversion mode

$$T_{Ps}(H, v_p, v_s, p) = H \left[\sqrt{\frac{1}{v_s^2} - p^2} - \sqrt{\frac{1}{v_p^2} - p^2} \right]. \quad (6)$$

176 Radial RFs at a single station in the depth domain are then linearly stacked to build the
 177 conversion response.

178 These methods are applied to broadband stations located in the eastern US (Fig-
 179 ure 1). This choice is motivated by the presence of seismic arrays with various station
 180 density and operation time that sample different geological settings. We investigate in
 181 particular the efficiency of the method for imaging a laterally variable crust underlying
 182 in places thick sedimentary basins (SB) such as in the Mississippi Embayment. Our data

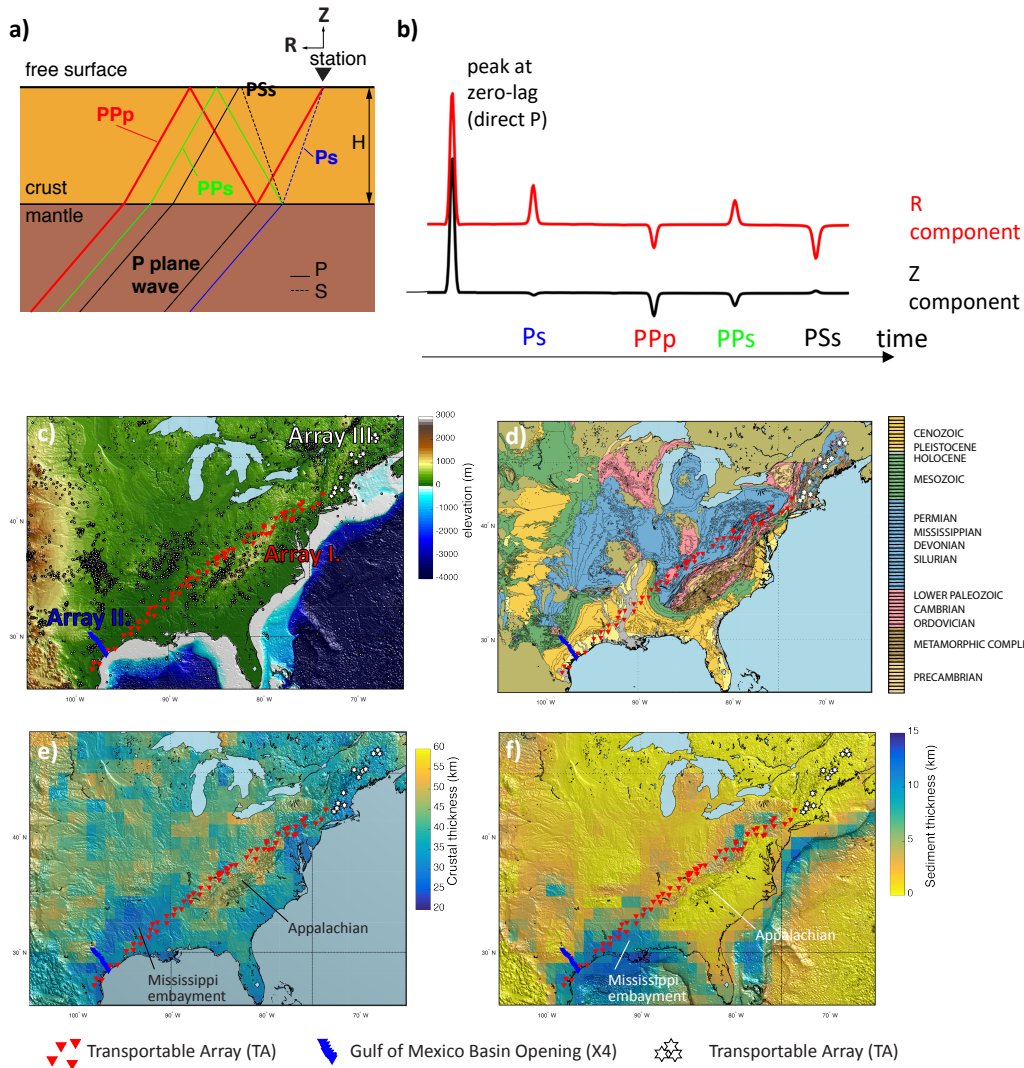


Figure 1. a) P-wave reverberations from teleseismic records. The seismic stations (black inverted triangle) sits on top of the crust (orange) above the mantle (brown). The thickness of the crust is denoted as H . P-wave is marked by solid lines and S-wave by dashed lines. The phases most relevant in this study are shown as P_s (blue), PP_p (red), PP_s (green), and PS_s (black). b) Vertical (black) and radial (red) responses of the ground below the receiver for a simple, one-layer crust. In the vertical RF, the PP_{mp} (PP_p) and PP_{ms} (PP_s) phases both exist but PP_{mp} is much stronger (Tauzin et al., 2019). c) Topography, together with seismic sub-arrays used in this study and the seismicity (black circles) from the USGS catalog. d) Main geological deposits color-coded as a function of age (P. G. Schruben et al., 1998). e) Seismic sub-arrays and crustal thickness taken from the globally compiled model CRUST1.0 (Laske et al., 2013). f) Sedimentary cover taken from CRUST1.0. The arrays belong to the following networks: Sub-Array I (red triangles) TA, Transportable Array; Sub-Array II (blue triangles) X4, Gulf of Mexico Basin Opening; Sub-Array III (white hexagrams) TA, Transportable Array.

183 are separated in three sub-arrays (Figure 1). We use the global crustal model Crust1.0
 184 (Laske et al., 2013) and the geology of the conterminous United States (King & Beik-
 185 man, 1974; P. G. A. Schruben et al., 1994) to describe the a priori structure beneath these

186 arrays (Figure 1). We benefit from the Transportable Array for constructing transects
 187 of the crustal structure over several thousand kilometers with an average inter-station
 188 spacing of 70 km (sub-arrays I and III). We distinguish Sub-Array I from III because they
 189 sample different geological structure. Sub-array I samples the thick sedimentary cover
 190 (up to 11 km) and thin crust (25-30 km) in the Mississippi embayment at southwest, and
 191 the western border of the Appalachian in the middle with a thicker crust (up to 50 km)
 192 and thinner sedimentary cover (3 km-thick) whereas sub-array III in Maine samples a
 193 standard crust (30 km thick) with no sedimentary cover. Finally, the Gulf of Mexico Basin
 194 Opening experiment (array II) is a linear array with 15 km inter-station spacing sam-
 195 pling sharp lateral changes of crustal and sedimentary thickness. Over 250 km, the model
 196 Crust1.0 indicates that the crust thins from 50 km at northwest to 35 km at southeast,
 197 and the sedimentary cover increases in thickness from 0 to 11 km. The 15-km inter-station
 198 spacing of sub-array II allows testing another imaging principle, Common Reflection Point
 199 (CRP) migration (Tauzin et al., 2019), which unfolds the information on the structure
 200 by projecting amplitude on the RFs onto the final leg of the path of reflected waves un-
 201 derneath the receivers (supplementary Figure S11).

202 The set of data used in this study is the same as used for classical radial RF stud-
 203 ies. Metadata and data are provided by the Incorporated Research Institutions for Seis-
 204 mology (IRIS) data center (DMC) (Ahern et al., 2007) and the Global Centroid Moment
 205 Tensor (GCMT) catalog (Ekström et al., 2012). We used three-component stations with
 206 the broadband channel BH, and selected events from the GCMT catalog with moment
 207 magnitudes larger than 5.5 and epicentral distances between 30 and 90° to avoid the ef-
 208 fect of triplications at mantle transition zone discontinuities and the core shadow zone.
 209 The processing is implemented using Matlab® scientific programming language, with the
 210 routine available at <http://perso.ens-lyon.fr/benoit.tauzin/data.htm>.

211 The seismograms were extracted and preprocessed to remove asynchronous records
 212 on the three components, resampled, and projected to the desired vertical-radial-transverse
 213 component orientations. We selected data with seismogram signal-to-noise ratio larger
 214 than 1.7, the signal and noise being measured from a root mean square over windows
 215 following ([0 3.25] s) and preceding ([-2.5 -0.5] s) the theoretical P-wave arrival (at 0 s)
 216 in the *iasp91* model (Kennett & Engdahl, 1991). The seismograms are pre-processed to
 217 start 20 s before the P-wave arrival with a duration of 80 s. The seismograms are then
 218 processed using equations (1) and (4), i.e. applying spectral whitening and autocorre-
 219 lation to build vertical RFs and water-level deconvolution for radial RFs.

220 The time-to-depth relationships, i.e. equations (3) and (6), are computed based on
 221 the velocity structure in the Crust1.0 model (Laske et al., 2013) at corresponding sta-
 222 tion locations. Crust1.0 is not taken here as providing the ground truth, but serves for
 223 a comparison with the observed data as well as guiding the interpretation of the recov-
 224 ered reflectivity. Crust1.0 is a global model that provides crustal types, thickness, and
 225 elastic properties of the crystalline crust according to basement age and tectonic setting
 226 (Laske et al., 2013). The Moho depth in particular is constrained by data from active-
 227 source seismic studies as well as radial RF analysis. So this model provides a good ref-
 228 erence for calibrating our seismic images and discussing the deviation of the first order
 229 structure from this model. The model in each cell is described as an eight-layer profile,
 230 including three sedimentary layers and three crustal layers. The parameters including
 231 P- and S-wave velocity, v_p , v_s , density, ρ and thickness, H , are given for each layer. Crust1.0
 232 is discretized over a $1 \times 1^\circ$ pixel spatial grid (Laske et al., 2013). We do not expect to re-
 233 cover exactly the same structure beneath stations that do not have contributed to the
 234 model. This is the case for array II, which is densely sampling the equivalent of ~ 2.5 cells
 235 of the Crust1.0 model (Figure 1). In all our applications, we compare the result of pro-
 236 cessing the observed data to synthetic data computed based on this global crustal model.
 237 We simulate the waveforms with the plane-wave matrix algorithm, “respknt” (Kennett,
 238 1983; Randall, 1989). Synthetics waveforms are computed for the same acquisition ge-

239 ometry as in the observed data and processed with the same strategy: filtering, auto-
240 correlation, time-to-depth conversion, and stacking. This approach is applied in all our
241 synthetic experiments (Figures 2, 6, 7, 9e, 10, 11, S4-S7), except Figure 9a-9d where the
242 slowness is 0.06 s/km.

243 For observed data, we found in a preliminary attempt that the selection based on
244 a signal-to-noise criterion applied on seismograms alone is not sufficient to ensure good
245 quality auto-correlation stacks. At frequencies investigated here, the noise on single au-
246 tocorrelations is a combination of incoherent (ambient) noise and signal-generated noise.
247 The signal-generated noise is a result of the teleseismic source function: it includes the
248 characteristics of the seismic source (slip history, radiation pattern, source spectrum) as
249 well as the effects of wave-propagation near the source. In addition, interfering phases,
250 such as PP or PcP, add complexity unrelated to the receiver-side structure. Stacking a
251 large number of data is required to decrease the noise level to acceptable level (Tauzin
252 et al., 2019). But because we use temporary arrays (Figure 1), the number of available
253 data is relatively small, which limits the performance of the stacking operation. Our ex-
254 periments showed that at stations with a small number of data, even an application of
255 a stacking with weighting based on the instantaneous phase (Schimmel & Paulssen, 1997)
256 is not able to provide satisfying results. We therefore discarded all stations with less than
257 10 (for sub-arrays I and III) or 15 (sub-array II) available autocorrelations.

258 We also relied on a more discriminative approach for data selection based on the
259 use of a "phasing depth diagram". We use trial depths of seismic interfaces (phasing depths)
260 and select traces that constructively contribute to the stacked signal at this depth. We
261 provide in Figure S1 an illustrative diagram of the procedure, and in Figures S2 and S3
262 two examples based on simple synthetic signals and field data, respectively. For a neg-
263 ative signal corresponding to an interface at X km depth, we first make a selection of the
264 traces with a negative signal within ± 5 km from X km depth. We then stack the selected
265 traces with bootstrap resampling. Because the traces are depth-converted, a successful
266 selection of traces contributing to build a signal at X km depth should contribute to align
267 (and build after stacking) signals for discontinuities at other depths. We retain only the
268 traces that contribute to these multiple depths. We show in Supplementary Material how
269 we use such a diagram juxtaposing stacked depth domain traces as a function of trial
270 depths (the phasing depth diagram) to select a distribution of good quality data for a
271 given station (supplementary Figures S1 and S3). This selective stacking method is more
272 efficient applied to vertical RFs than to regular radial RFs. The reason is that the method
273 focuses on removing the effect of random noise, but not coherent noise components. In
274 regular radial RFs, a coherent noise component dominates, which is the structure-generated
275 signal due to reverberations in the shallow sedimentary cover.

276 Supplementary tables S1-S3 provide for the three sub-arrays the final number of
277 RFs obtained at each station.

278 **3 Synthetic experiments**

279 We present in Figure 2 the Crust1.0 structure and corresponding synthetic radial
280 and vertical RFs for selected stations ordered by increasing thickness of the sedimentary
281 cover in Crust1.0. Radial RFs have been computed through water-level deconvolution
282 following equations (4)-(5) (Figure 2b). Vertical RFs are calculated using autocorrela-
283 tion and spectral whitening following equation (1)-(2) (Figure 2c). Generally, the ver-
284 tical RFs provide good predictions for the Moho depth for all selected stations for all the
285 velocity models. However, the radial RFs are more complicated. For a crustal cover with-
286 out sedimentary basin (P56A), the 'Moho pulse' appears at the true depth and is reli-
287 able. For a thin sedimentary cover (QUA2), oscillations due to reverberations are very
288 strong at shallow depth, while the 'Moho pulse' can still be distinguished in the radial
289 RF. The converted pulses are followed by short duration and low-amplitude oscillations

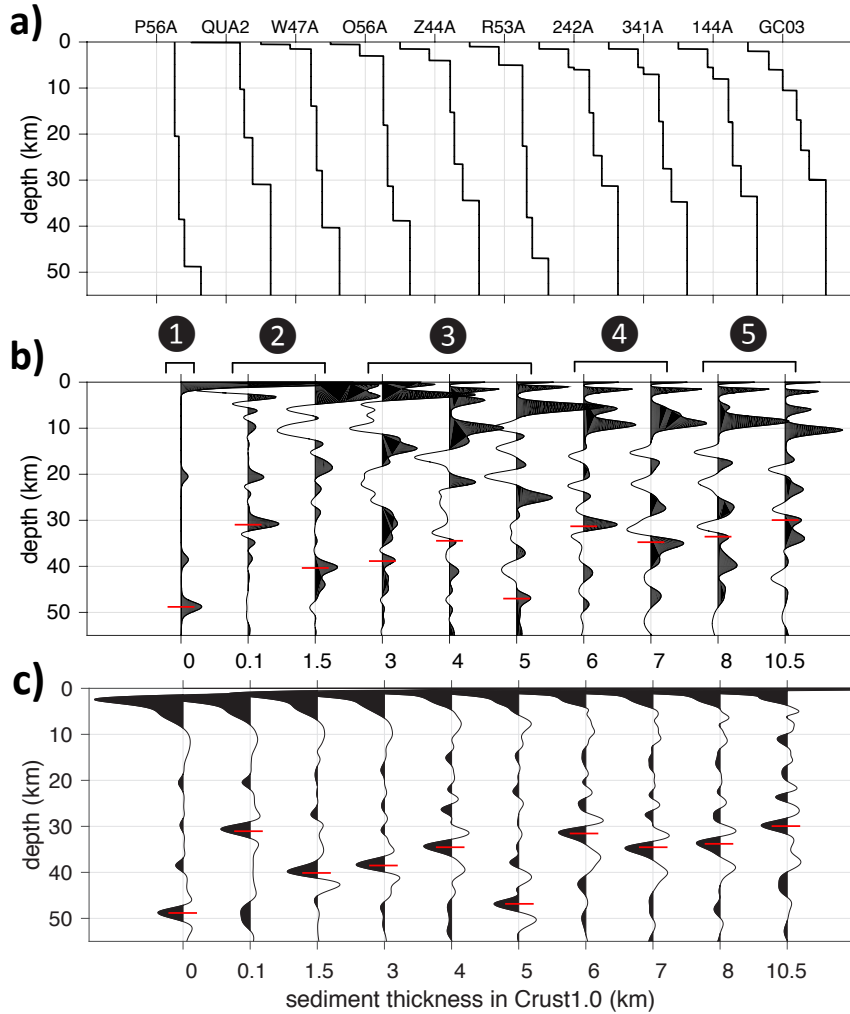


Figure 2. Reference P-wave velocity profiles (a) and corresponding synthetic radial (b) and vertical receiver functions (c) for 10 selected stations with increasing thickness of the sedimentary cover according to Crust1.0. The red lines indicates the Moho depth in Crust1.0. The vertical RFs are processed with $W = 0.1$ Hz.

290 associated with post-cursory shear-wave reverberations of the converted wave in the thin
 291 sedimentary layer. For thicker sedimentary covers, the ‘Moho pulses’ are not reliable any-
 292 more. The pulses result from the interference of conversions at the Moho discontinuity
 293 and multiple reverberations (Figure 2b, station sets 3, 4 and 5). The Moho pulse can-
 294 not be distinguished from shallow multiples. In addition, the maximum amplitude on
 295 the radial RF is not the P-wave peak but the conversion at the base of the basin. This
 296 suggests that vertical RFs as processed here will be a more reliable source of informa-
 297 tion about the deep crustal structure than radial RFs.

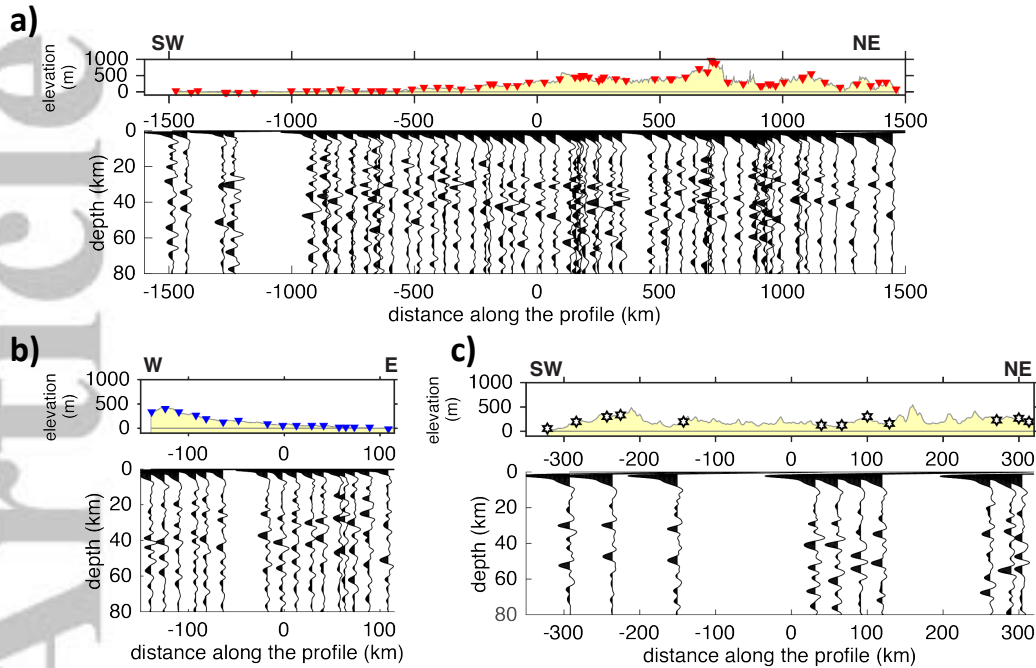


Figure 3. P-wave auto-correlation signals (black traces) along the three sub-arrays in Figure 1c. The arrays are (a) sub-array I, (b) sub-array II, and (c) sub-array III. The top panel in each sub-plot presents the topographic profile (Smith & Sandwell, 1997), with markers positioning seismic stations. The bottom panels are the observed autocorrelograms (black traces) in the depth domain. To target the Moho, the vertical RFs are processed with $W = 0.1$ Hz and a post-processing filter with 0.2-1.0 Hz bandpass.

4 Results

4.1 Results for the three sub-arrays

We show in supplementary Figures S5, S6, and S7 examples of vertical RF stacks for three selected Transportable Array stations from sub-array I. For these stations, and despite a two-year duration of acquisition, there is no apparent loss in quality of the stacked autocorrelograms with respect to a permanent station such as HRV (Figure S4). The data selection slightly improves the lateral continuity of signals when building a profile from stations with variable numbers of earthquake records (Figure S8). For 71 stations in sub-array I, 10 stations have a set of less than 15 RFs, which are discarded, and among the remaining 61 stations, 43 stations have no more than 50 waveforms. The application of bootstrap resampling allows to estimate the variability of stacked waveforms and demonstrates that we observed robust signals (supplementary Figure S9).

Overall, the vertical RFs are relatively simple with 2, at maximum 3, major pulses (Figure 3). This is in contrast with the radial RFs, which show significantly more complexity (see section 5.2 in discussion; Figure 7). Chains of pulses are consistently observed along the three profiles at ~ 30 km and ~ 40 km depth (Figure 3), likely associated with the deepest crustal layering. Yet, it can be relatively complicated to interpret vertical RFs in terms of a deterministic structure. Multiple arrivals with similar amplitudes are recovered at crustal levels, making the identification of the Mohorovičić discontinuity ambiguous. In some cases, arrivals are detected at lithospheric mantle depth, for example at the southwestern portion of sub-array III (Figure 3c), where the Moho is not expected

319 to lie deeper than 35 km according to Crust1.0 (Figure 1e). Although we cannot take
 320 the structure provided by Crust1.0 as the ground truth, we can interpret this deep signal
 321 as a fictitious interface that results from the arrival of multiple reverberations with
 322 cross-mode coupling, PPs (see Figure 1a, b and synthetic experiment based on Crust1.0
 323 in section 4.2).

324 A priori geological and seismological information show that major holocene to ceno-
 325 zoic sedimentary basin structures are sampled by sub-array I and II (Figure 1d, f). Yet,
 326 we do not observe significant lateral variations of signal quality when the arrays cross
 327 such structures (Figure 3a). We will show in section 5.2 that this is a clear advantage of
 328 the vertical RFs over the traditional radial RF method.

329 4.2 Comparison with Crust1.0

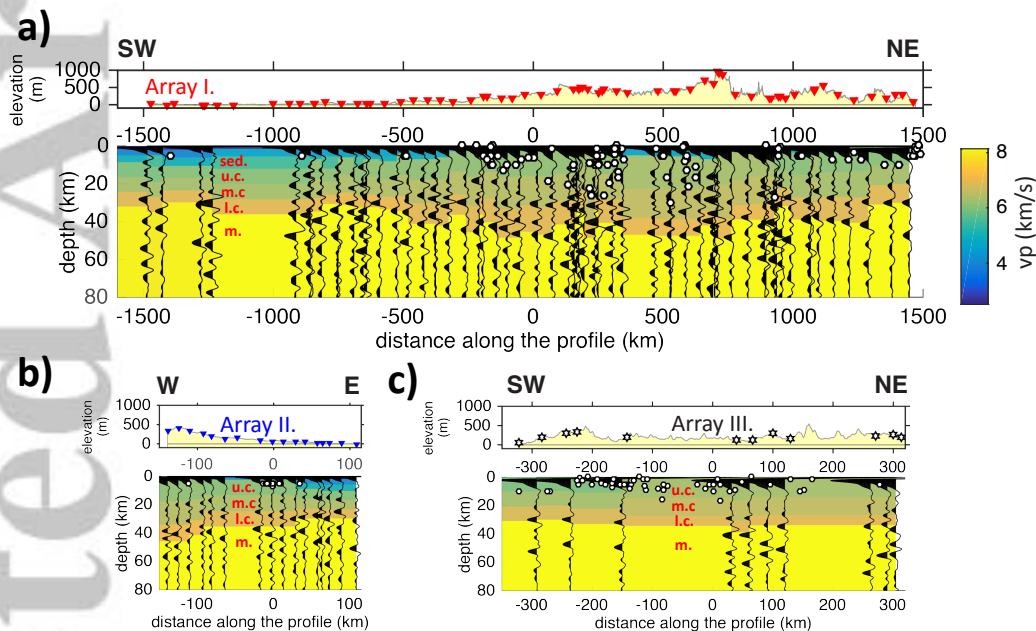


Figure 4. Superimposition of observed P-wave auto-correlation signals (black traces) to the P-wave velocity structure (background colors) in the reference crustal model Crust1.0 (Laske et al., 2013). The white circles are associated with the local seismicity (USGS catalog; see Figure 1c). The layers are sed. (sedimentary layers), u.c. (upper crust), m.c. (middle crust), l.c. (lower crust), and m. (mantle).

330 We first use Crust1.0 as a reference crustal model for comparison, but not acting
 331 as constraint to interpret crustal structures. In a second step, we use Crust1.0 as a guide
 332 for identifying and picking the Moho interface on vertical autocorrelations. Autocorrelations
 333 are plotted against Crust1.0 P-wave velocities in the background of Figure 4. The
 334 three sedimentary basin layers are marked with dark blue colors (sed.), the crustal layers
 335 as light blue to brown (upper, mid and lower crust; u.c., m.c. and l.c.), overlying the
 336 mantle (m.) in yellow. This a priori seismological structure allows a more confident interpretation
 337 of the horizons detected with vertical autocorrelations. In all three profiles, we observe a rough
 338 agreement between the large negative peaks in observed data and the velocity model. There is good
 339 but not perfect agreement between the strongest amplitude negative pulses observed on autocorrelations
 340 and the base of the crust (brown-to-yellow transition). We find that the northeast portion of sub-array I
 341 and sub-array

342 III both produce the best match with the Moho depth in Crust1.0, where the crust con-
 343 tains no sedimentary layers and is the most laterally homogeneous.

344 We propose in Figure 5a a guided picking of interfaces of the crust, where the purple
 345 horizon represents the Moho discontinuity and the shallower blue horizon an intra-
 346 crustal discontinuity. We demonstrate here that extracting coherent information about
 347 P-wave reflections from event-based vertical RFs/autocorrelations computed from tem-
 348 porary networks and dense arrays is feasible. The continuous horizon between 20 and
 349 30 km depth on the profile obtained from sub-array I in blue (Figure 5) is consistent with
 350 a reflective interface at the top of the lower crust. A number of arrivals at shallower and
 351 deeper levels have low-amplitude and/or poorer lateral continuity, so are more difficult
 352 to interpret. The comparison between Figures 4 and 5 suggests that Transportable Ar-
 353 ray data are of sufficient quality to highlight with autocorrelations the crustal internal
 354 stratification.

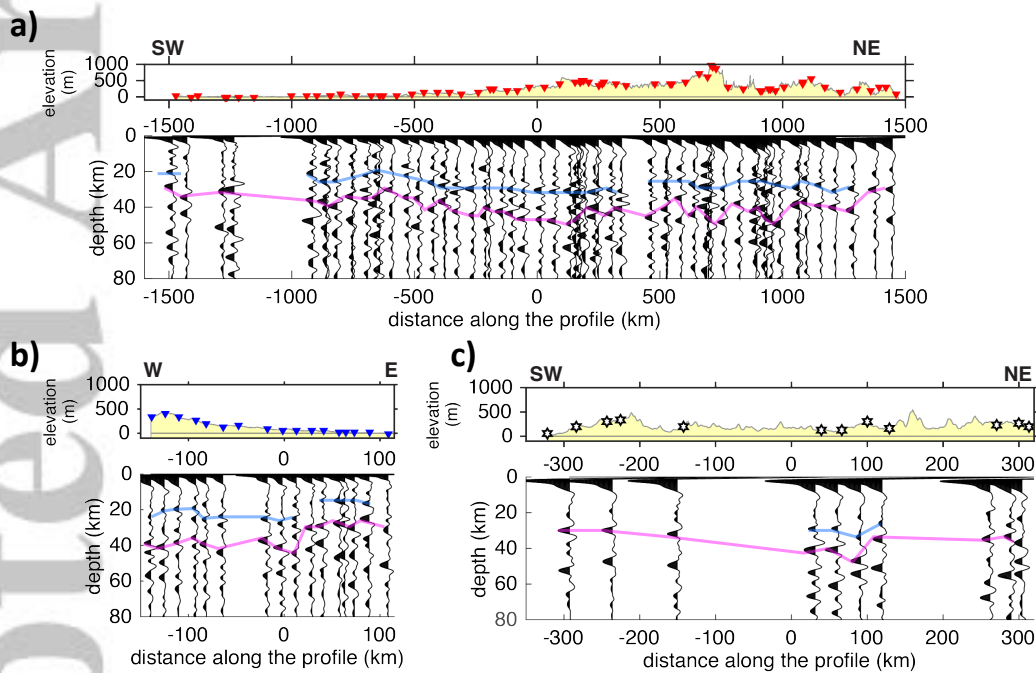


Figure 5. The same as Figure 3, but now with the proposed picks of laterally continuous crustal interfaces. The light purple horizon represents the Moho discontinuity and the shallower, blue horizon, an intra-crustal discontinuity.

355 However, there are differences (Figure 4): (i) there exist minima and maxima in
 356 the vertical RFs that are not associated with discontinuities as described by Crust1.0,
 357 in particular, in the lithospheric mantle; (ii) many small amplitude arrivals might cor-
 358 respond to features present in the Crust1.0 model but are slightly offset, (iii) along the
 359 250 km extent of the linear sub-array III, the data reveal variations of Moho topogra-
 360 phy (Figure 4b) that are not present in the model, (iv) at depths < 10 km, the response
 361 loses its interpretability as it appears dominated by signal-processing artifacts.

362 For further comparison, we computed the synthetic vertical RFs for the Crust1.0
 363 model with the same acquisition geometry as observed in the data (Figure 6). This syn-
 364 thetic experiment demonstrates that vertical RFs are fairly simple and, in theory, most
 365 of the predicted pulses can be deterministically attributed to interfaces in the input model,
 366 although some secondary arrivals at crustal depth and in the uppermost mantle can be

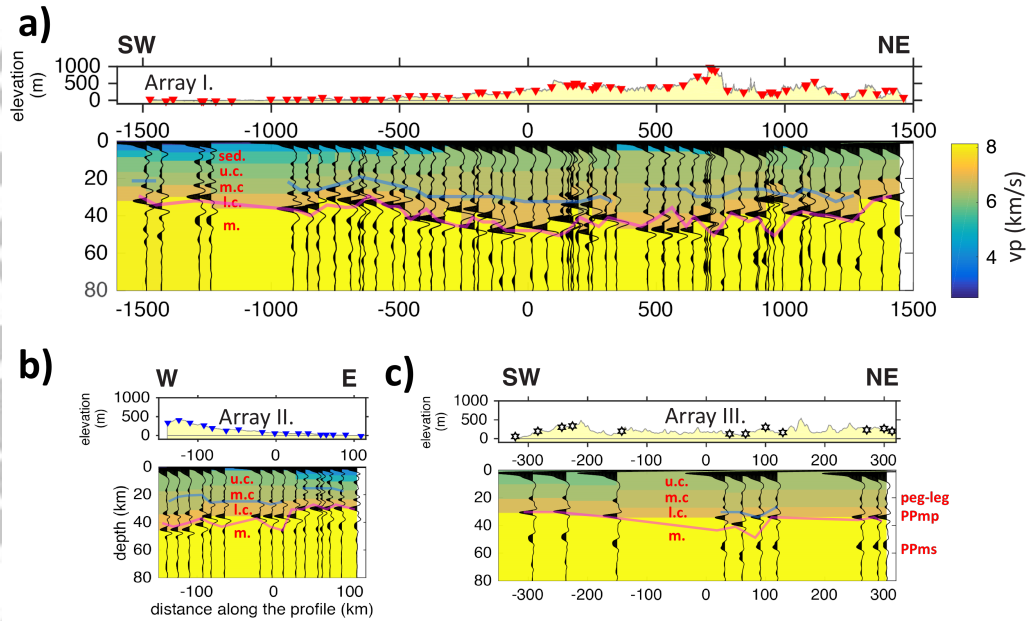


Figure 6. Superposition of synthetic P-wave auto-correlation signals (black traces) to the P-wave velocity structure (background colors) in the global crustal model Crust1.0 (Laske et al., 2013). The light purple and blue horizons are same as Figure 5.

367 attributed to “peg-leg reverberations” or cross-mode contamination (PPms). In addition,
 368 this synthetic experiment shows that the method, with this choice of parameters
 369 ($f_{min} = 0.2$ Hz and $W = 0.1$ Hz), suffers from a loss in resolution at shallow depth
 370 (< 10 km). This is the result of the pronounced side-lobe of the peak at zero-lag in the
 371 autocorrelations.

372 We can draw three important conclusions from the comparison of Figures 4 and
 373 6. Firstly, observed vertical autocorrelations are more complex than predicted based on
 374 Crust1.0, suggesting that there exist at crustal level small-scale heterogeneities and/or
 375 3D effects of wave-propagation that are not captured using the reference model. Secondly,
 376 our method successfully recovers the crustal information without loss of signal-to-noise
 377 ratio or increased complexity in regions with thick sedimentary cover. This latter conclusion
 378 is supported by both the synthetic and observed data in the southwest portion
 379 of sub-array I and eastern portion of sub-array II (Figures 4 and 6). Finally, in the observed
 380 data, P-wave reflections from the top of the Moho discontinuity are consistently
 381 observed with lower amplitudes than predicted by the Crust1.0 model (Figures 4 and
 382 6). In contrast, reflected pulses associated with intra-crustal discontinuities have a similar
 383 or slightly higher amplitude than predicted by Crust1.0.

384 Supplementary Fig. S10 shows a negative correlation (-0.58) between our observed
 385 crustal thickness and the thickness of the sedimentary cover in the Crust1.0 model. This
 386 anti-correlation is predicted for a crust in isostatic equilibrium. The fit of a theoretical
 387 model to our best fitting line is obtained for a sediment density of 2.15 g/cm³, which is
 388 within the continental average range of densities for soft (2.07 g/cm³) and hard (2.38
 389 g/cm³) sediments in the Crust1.0 model (Laske et al., 2013).

5 Discussion

5.1 On the interpretation of autocorrelations

As presented in our results section, we unambiguously identify two chains of pulses near 30 and 40 km depth. From synthetic experiments and using of independent information (Crust1.0 model), we demonstrated that these chains of pulses are related to the reflections from the upper side of the Moho discontinuity, namely PPmp and PPms, and from the top of the lower crustal layer. Due to the limited number of data and intrinsic characteristics of the Moho boundary (see section 5.4), it can, however, be challenging to unambiguously pick the PPmp phase on autocorrelations. This is not a unique problem to our particular dataset, as most other prior studies based on autocorrelations suffer from similar interpretation problems (cross-mode contaminations and narrow frequency band limiting the resolution of velocity gradients) (e.g., Tibuleac & von Seggern, 2012; Gorbato et al., 2013; Sun & Kennett, 2016; Taylor et al., 2016; Saygin et al., 2017; Becker & Knapmeyer-Endrun, 2018). In addition, we show in next section that the vertical RFs behave better than radial RFs in the presence of a sedimentary cover. We therefore cast our analysis as a reference for future interpretations based on this technique.

Tauzin et al. (2019) showed that the lateral sampling of the P_{pp} mode increases with the depth of investigation, and the difference with typical P_s conversion modes used in the radial RF imaging is of the order of 5 km at the depth of the Moho. This means that, in the single-station stacking, the cone of sensitivity of the P-wave reflections surrounding the stations will have a 10 to 20 km diameter (this distance is slowness-dependent) while it will have only a 5 to 10 km diameter for the P_s conversions. As such, station-based gathering will be slightly more vulnerable to the presence of strong lateral variations in the Moho depth (crustal thickness) than in the radial RF imaging.

The effect will be a slight decrease in amplitude of the reflected phase due to out-of-phase stacking. In addition to lateral variations of the Moho, crustal heterogeneity and surface topography both contribute to the PPmp-P differential travel time. The maximum topographic difference in our study is about 1 km. We estimate the delays introduced by a 1-km topography of the Earth surface and at the Moho discontinuity to be 0.8 s and 0.3 s respectively. Such delays are significant, but smaller than the width of the reflected pulse (1s). Consequently, if topographic variations over the area surrounding the station may contribute to the decrease in amplitude of the PPmp reflected pulse, they are unlikely to explain the whole difference with Crust1.0. This conclusion is also supported by the observation that the PPmp amplitudes are remarkably consistent across all of our images, and appear uncorrelated with local gradients in surface topography. An additional strong argument for a negligible effect of surface topography is the observation of the reflections from the top of the lower crust with amplitudes similar as predicted by model Crust1.0. We conclude that the difference between the observed and the Crust1.0 Moho amplitudes must therefore have another origin (see section 5.4).

In supplementary Figure S11, we present an image of the crustal structure along the sub-array II based on the common reflection point stacking method (Tauzin et al., 2019), accounting for the geometry of illumination of the structure by the P_{pp} mode. Sub-array II is better positioned for performing such an experiment as the inter-station distance is the smallest among the three subarrays considered here. The image remains consistent with the observed structure from the single-station stacking, although the portions of the image with poor ray coverage suffer from a low signal-to-noise ratio.

5.2 Radial receiver functions

We present in Figure 7 stacked radial RFs for the three sub-arrays. Corresponding seismic sections are shown for the observed data and for the predictions from Crust1.0, both superimposed to the v_p structure in Crust1.0. Because each interface generates a

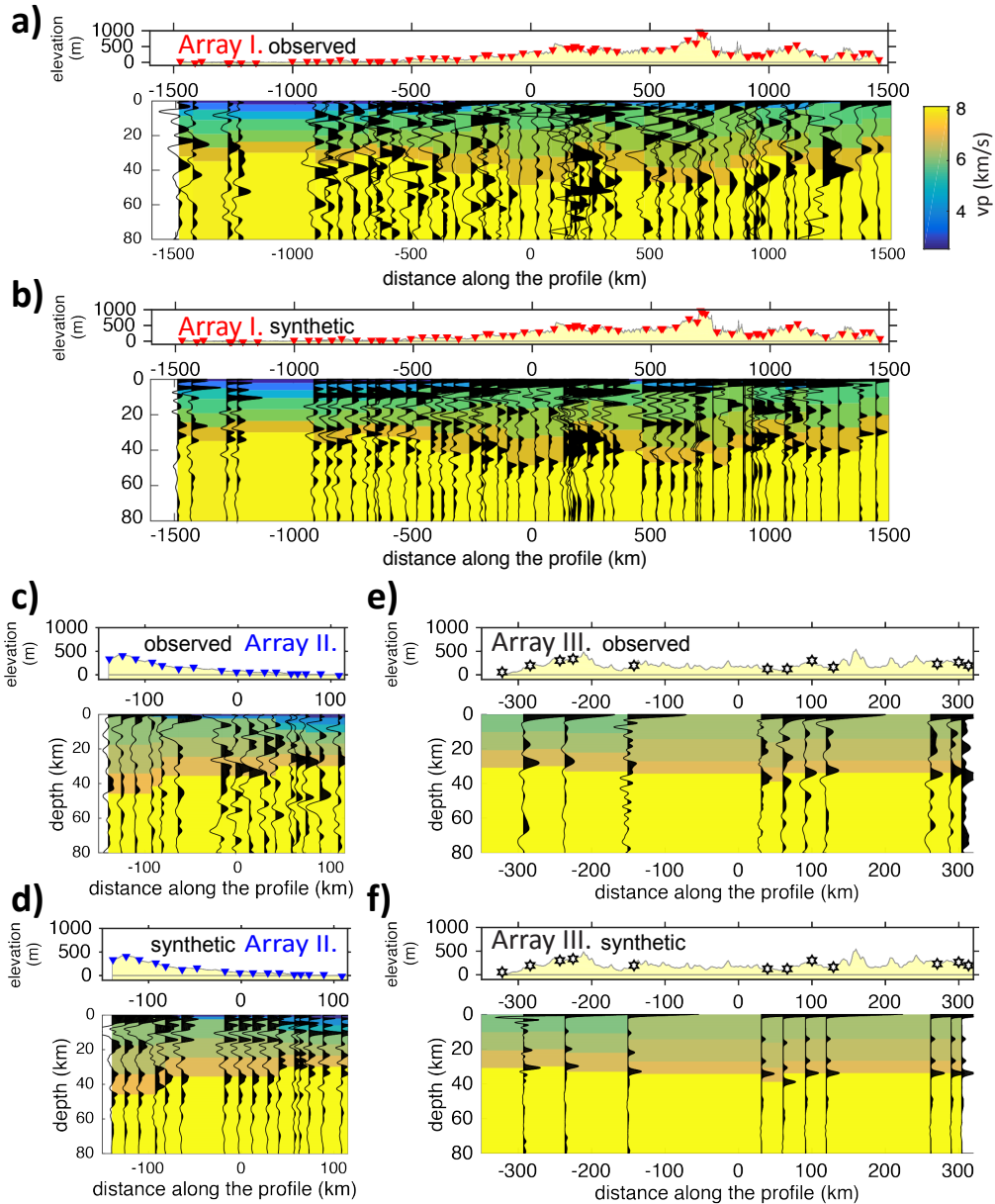


Figure 7. Observed (a, c, and e) and synthetic (b, d, and f) radial receiver functions (black traces) superimposed to the P-wave velocity structure (background colors) in the global crustal model Crust1.0 (Laske et al., 2013). Panels the others are synthetics. No post-processing filtering is applied.

440 triplet of phases (Ps, PP_s, PS_s), the crustal structure has less readability than in the case
 441 of vertical RFs, even in the synthetic case (compare Figure 7b to 6a). The simplest ra-
 442 dial RFs are obtained for sub-array III because the crust does not include a near-surface
 443 sedimentary cover. In this case, the Moho has the strongest amplitude and the maxima
 444 of converted Ps pulses can easily be associated with crustal interfaces (Figure 7e-f).

445 When one or several low-velocity sedimentary layers are present, radial RFs get more
 446 complicated. Instead of being dominated by positive pulses associated with increases of

447 velocity/impedance at intra-crustal discontinuities (Figure 7e, f), radial RFs incorpo-
 448 rate a strongly oscillating component (Figure 7a-d) with unreliable converted pulses as-
 449 sociated with the Moho discontinuity. This behavior is easily explained by the synthetic
 450 experiment shown in section 3. In conclusion, even in absence of noise of natural origin,
 451 the radial RFs are less reliable tools than the vertical RFs when low-velocity sedimentary
 452 layers exist near the surface. In comparison, the vertical RFs are simpler to inter-
 453 pret, although it is fair to say that they are not void of artifacts related to these shall-
 454 low reverberations. We discuss the effect of reverberations and sedimentary basin struc-
 455 ture in section 5.3, together with the impact of playing with the width of the smoothing
 456 window W for spectral whitening. We show in particular that a well-chosen value
 457 of W significantly improves the readability of the crust because spectral whitening can
 458 act as a resonance removal filter.

459 5.3 Filtering out basin resonance through spectral whitening

460 In sedimentary basins, a strong resonance effect is recorded on the vertical com-
 461 ponent as P-wave reverberates multiple times in the low-velocity sedimentary cover. Fig-
 462 ure 8 shows the sequence of P-wave reverberations in a simple sedimentary structure,
 463 with a single layer. The sedimentary layer has lower velocities than the half-space be-
 464 neath it. Teleseismic P waves reach the basement of the sedimentary layer and trans-
 465 mits as first-order P waves. The reflection of P waves at the free surface is a total re-
 466 flection. Due to the significant impedance contrast at the base of the sedimentary layer,
 467 the free surface reflected P-waves reverberate multiple times inside the sedimentary layer.
 468 These reverberations contribute to a strong resonance effect, which is recorded by the
 469 receiver on the Earth's surface mainly on the vertical component. In the time domain,
 470 these reverberations correspond to strong amplitude pulses that contaminate the seis-
 471 mograms. A remark is that on the vertical component, interference effects from converted
 472 S-waves are small because of the extremely low-incidence angle of P-waves due to the
 473 slow velocities in the SB layer.

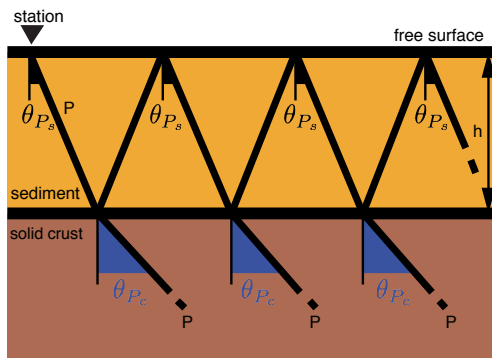


Figure 8. Sequence of reverberations in a sedimentary layer. The seismic station (black inverted triangle) sits on a sedimentary layer (orange) above the solid crust (brown). The direct P wave reaches the discontinuity between the sedimentary layer and the solid crust, and generates a first-order P wave. Due to the significant impedance contrast, the first-order P waves reverberate multiple times inside of the sedimentary layer. The thickness of the sedimentary layer is denoted as h . θ_{P_c} and θ_{P_s} are the incident angles of P waves in the crust and sediment layer respectively.

To understand the reverberations caused by SBs, we use an example with a sedimentary layer over a half space bedrock. The power spectrum of an impulse wavefront

at normal incidence through a sedimentary layer over a half space bedrock can be expressed as,

$$|Z(f)| = \frac{1-r}{1+r} \cdot \frac{1}{(1+(re^{-2\pi fQ})^2 - 2re^{-2\pi fQ} \cos 2\pi f\tau)^{\frac{1}{2}}}. \quad (7)$$

474 where details can be referred to Appendix A in Pham and Tkalčić (2018) for the full deriva-
 475 tion of Equation 7 using the matrix propagation method (Claerbout, 1968; Kennett, 1983).
 476 In Equation 7, $r = (\rho_s v_s - \rho_c v_c) / (\rho_s v_s + \rho_c v_c)$ is the reflection coefficient at the sedi-
 477 mentary basin-crust interface in downward direction. ρ and v are density and wave speed
 478 of the media, where subscript $_s$ refers to the sedimentary basin and $_c$ to the crustal rock.
 479 $\tau = 2h/v$ is the two-way travel time in the layer. Q is the attenuation factor of in the
 480 sediment layer.

The spectral response in Equation 7 is a function in the frequency domain, which is characterized by peaks that are equally spaced at resonance frequencies,

$$f_n = \left(n + \frac{1}{2}\right) \cdot \frac{1}{\tau}. \quad (8)$$

481 Despite the fact that Equation 7 is derived for normal incidence, it represents a good ap-
 482 proximation for slight oblique incidence (see Figure S12 in the supplement). This shows
 483 that the contribution of converted S wave on the vertical component in slightly oblique
 484 incidence is negligible.

485 In equation (2), the frequency-dependent spectral-whitening operation allows bal-
 486 ancing the frequency content of the RFs (Bensen et al., 2007; Pham & Tkalčić, 2017; Tauzin
 487 et al., 2019), and also removing specific spectrum-maxima related to the resonance of
 488 the layered structure beneath a receiver. To illustrate this, we proceed with a numer-
 489 ical experiment with simple one-dimensional models (Figure 9). The first model has a
 490 one-layer crust (no SB). The second model has a two-layer crust including a layer near
 491 the surface with low-velocities mimicking the effect of a sedimentary cover (SB model).
 492 This layer is 2 km thick. The Moho is located at 30 km depth in both models. The elas-
 493 tic parameters chosen for the SB layer and the contrast in impedance across its base are
 494 consistent with the structure given for station QUA2 in Crust1.0.

495 We simulate vertical-component waveforms with the same plane-wave matrix al-
 496 gorithm (Kennett, 1983; Randall, 1989). Figure 9b shows the results of the numerical
 497 experiment in the time-domain for vertical component waveforms. In addition to the peak
 498 at zero-lag, the black trace (no SB model) shows the pulses of the P-wave reflection at
 499 the Moho (PPmp). For the SB model (red trace), the large contrast of elastic proper-
 500 ties at the base of the SB introduces a strong resonance effect which contaminates the
 501 seismic response. This resonance corresponds to the ringing due to P-wave reverbera-
 502 tions in the shallow sedimentary layer (Equation (7)). This makes it difficult to distin-
 503 guish the reflection at the base of the crust (Figure 9b). In the frequency domain (Fig-
 504 ure 9c), the fundamental-mode resonance on the red spectrum appears as a broad and
 505 strong amplitude peak centered at ~ 0.3 Hz, consistent with the 2-km thick, near-surface
 506 layer according to equation (3).

507 Spectral whitening offers a way to turn off such a resonance. The first step con-
 508 sists in smoothing the vertical component spectrum running an average over the pre-defined
 509 width W . We use $W = 0.1$ Hz in this example (Figure 9c). The smoothed spectrum
 510 (green) only preserves the broad peaks due to resonance in the shallow sedimentary layer.
 511 The deconvolution in the frequency domain (Equation (1)) gives a spectrum close to the
 512 model without SB (Figure 9d), and the exponentially-decaying ringing is partially re-
 513 moved from the corresponding time-domain trace (Figure 9b). The whitened SB trace
 514 can now be interpreted, in particular to find the phase reflected at the Moho disconti-
 515 nuity. A residual ringing persists because the spectral whitening does not completely fil-
 516 ter out the effect of the shallow SB on the vertical component spectrum.

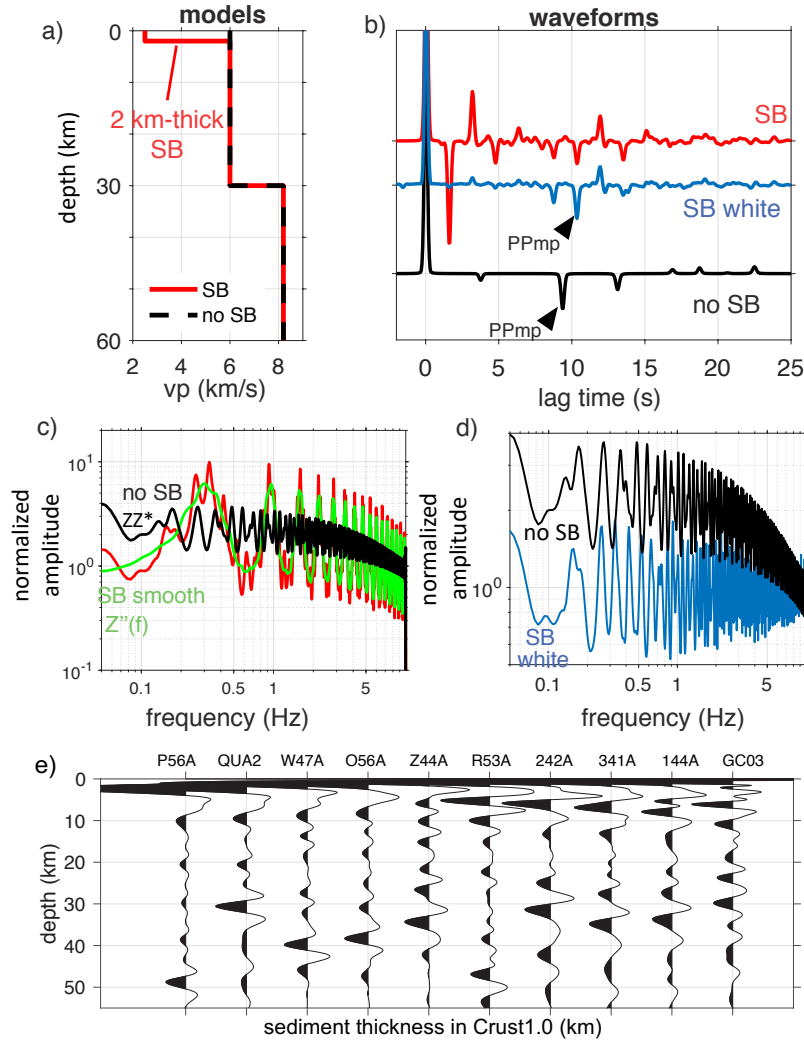


Figure 9. Numerical experiment illustrating turning off the resonance associated with a shallow sedimentary layer. (a) Crustal velocity models with a "normal" crust (no SB) and a sedimentary basin (SB model). (b) Simulated vertical responses aligned by P-wave arrival. The black seismogram is the vertical response for the normal crust (no SB). The red one is for the sedimentary basin (SB model). The blue one is the result of spectral whitening for the SB model (SB white). Major identified phases are the P-wave reflections (PPmp) and the P-to-S reflection (PPms) above the Moho. The slowness $p = 0.06$ s/km. (c) Spectra $Z(f)$ of the vertical component responses. The spectra in black and red represent the responses ZZ^* for the normal crust (no SB) and sedimentary basin (SB model) respectively. The spectrum in green represents the smoothed response $Z''(f)$ for the SB model. (d) The spectrum after spectral whitening for the SB model (blue), compared with the spectrum for the "normal crust" model (black). (e) Synthetic vertical autocorrelations for the same 10 stations as in Figure 2 computed with $W=0.4$ Hz. Combined with Figure 2c, this figure shows filtering-on or -off the resonance in the shallow sedimentary cover with different value of smoothing parameter W .

517

518

Figures 9e and Figure 2c compare synthetic vertical autocorrelations for the various structures shown in Figure 2a, and show the effect of choosing different values of

519 W . Choosing a large value of W (here $W = 0.4$ Hz) corresponds to applying the au-
 520 tuncorrelation method without turning on the resonance removal filter (Figure 9e). When
 521 using $W = 0.1$ Hz, oscillations associated with SB reverberations are damped, and this
 522 eases the interpretation of the crustal structure (Figure 2c). In general, $W=0.1$ Hz is a
 523 reasonable value to choose when targeting a Moho near 35 km depth.

524 Initially designed for improving the resolution of autocorrelations (Pham & Tkalčić,
 525 2017), spectral whitening is a simple method that also acts as a resonance removal fil-
 526 ter. Here, we demonstrate that spectral whitening can effectively remove the resonance
 527 associated with SB. There exists other methods performing such a function. For exam-
 528 ple, Yu et al. (2015) used RFs to determine the crustal structures for seismic stations
 529 on top of a low-velocity sedimentary layer. They applied autocorrelation with a resonance
 530 removal filter in the frequency domain to reduce the amplitude of reverberations in the
 531 layer. Langston (2011) used downward continuation and wave-field decomposition to re-
 532 duce the effect of SB reverberations. This method requires a prior knowledge of the Earth
 533 structure and modeling to extract Ps conversions from the deeper crust. Tao et al. (2014)
 534 used wavefield downward continuation to estimate sedimentary and crustal structure.
 535 The same authors used the H- κ grid searching technique to study the Moho depth and
 536 average V_p/V_s ratio. They applied H- β method to remove the reverberations caused by
 537 unconsolidated sediments. Yang and Niu (2019) studied sedimentary structure of basins
 538 in China from frequency dependent P-wave particle motion. Li et al. (2019) successfully
 539 isolated the Moho P-to-S conversion from sediment reverberations with a wavefield-downward-
 540 continuation technique. They reported a joint inversion that can retrieve the input sed-
 541 imentary models. A comprehensive comparison between these methods and the resonance
 542 removal filter described here would be interesting but is out of the scope of this study.

543 5.4 The Moho as a transitional layer

544 In high-frequency (> 10 Hz) active seismic reflection experiments, it is common to
 545 observe a laterally variable crustal reflectivity between geological terraces, but also a
 546 vertical contrast in reflectivity at the transition between the crust and upper mantle (e.g.,
 547 Kennett & Saygin, 2015). The Mohorovičić discontinuity is regularly identified as the
 548 base of the lower crust, but is often itself not marked by a strong reflectivity. The up-
 549 per mantle shows no distinct reflections probably because the vertical scale of the struc-
 550 ture is longer than the seismic wavelength used in active reflection surveys (Kennett &
 551 Furumura, 2016). At the same time, seismic surveys based on radial RFs with lower fre-
 552 quency content (< 1 Hz) point at the Moho being the most reflective interface.

553 The Moho is a first-order discontinuity in Crust1.0 with contrasts of $\sim 16\%$ in v_p
 554 and $\sim 13\%$ in v_s and density. Here, we find that amplitudes of low-frequency (0.2-1.0 Hz)
 555 P-waves reflections on top of the Moho, measured using autocorrelations (Figure 4), are
 556 weaker than predicted by the Crust1.0 model (Figure 6). We discussed in section 5.1 the
 557 effects of surface and boundary topography, pointing that these are unlikely explanations
 558 for such weak amplitudes. We here consider three alternative scenarios: (i) the elastic
 559 impedance contrast at the boundary is smaller than predicted by Crust1.0, (ii) there is
 560 an effect of anelasticity that is not accounted for in the seismic modeling, and/or (iii)
 561 the Moho is a transitional layer rather than a sharp boundary. The first scenario is un-
 562 likely as a smaller impedance contrast would lead to decreased Ps conversion amplitudes
 563 on radial component RFs as well. Nonetheless, where observed, the pulse of the direct
 564 Moho Ps (Figures 7a, c, and e) conversion has a similar amplitude as predicted by Crust1.0
 565 (Figures 7b, d, and f). For the same reason, the second case is unlikely. The effect of at-
 566 tenuation is expected to be stronger on shear-waves than on P-waves, thus should affect
 567 more responses on the radial components.

568 For petrological reasons, the seismic Moho is likely a gradual transition (e.g., Fur-
 569 long & Fountain, 1986; White & McKenzie, 1989; Arndt & Goldstein, 1989; Dufek & Bergantz,

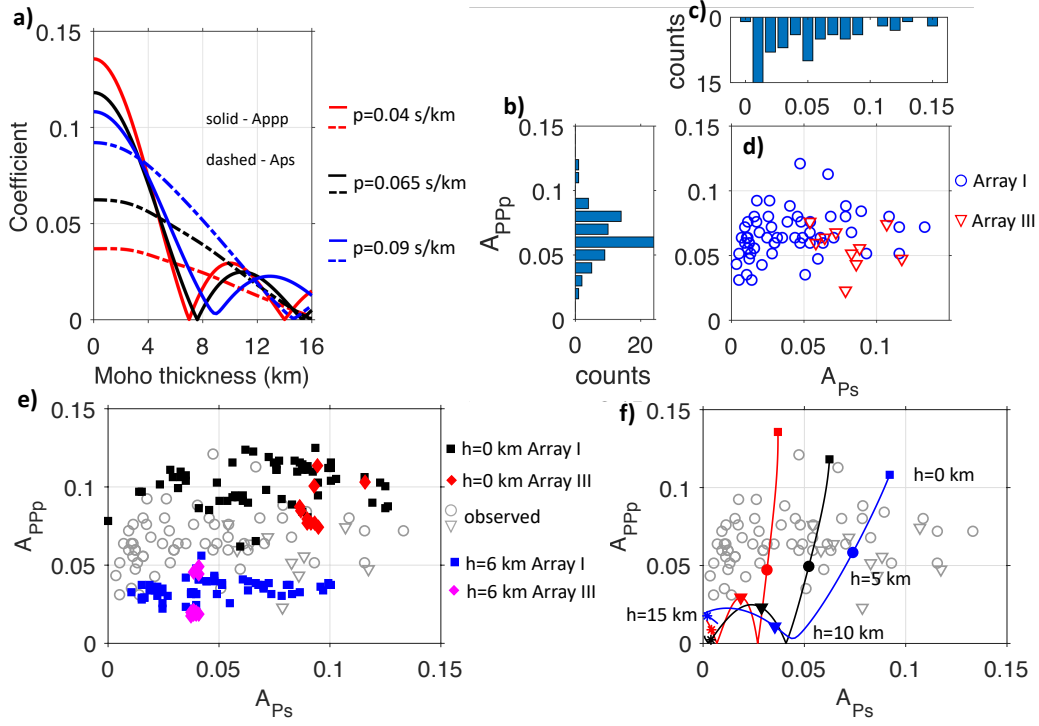


Figure 10. Sensitivity of PPmp reflections and Pms transmissions to a gradual Moho layer. (a) Variation of the topside P-wave reflection coefficient R_{pp} (solid lines) and bottom-up transmission coefficient T_{ps} (dashed lines) with the thickness of the velocity gradient at the Moho. Coefficients are calculated for a P plane wave with different slowness: $p = 0.04$ s/km (red), $p = 0.065$ s/km (black), and $p = 0.09$ s/km (blue). Here, the elastic properties across the Moho is defined by Crust1.0 for station KVTX in sub-array I. The value of coefficient is taken in the middle of the frequency band used in an analysis of vertical RFs (0.2 -1.0 Hz). (b) Histogram of measured amplitude of reflections (A_{PPp}) for sub-arrays I and III. (c) Histogram of measured amplitude of conversions (A_{Ps}) for sub-arrays I and III. (d) Measured amplitudes of reflections (A_{PPp}) as a function of amplitudes of transmissions (A_{Ps}) for observed data of sub-arrays I (blue circles) and III (red triangles). (e) A_{PPp} v.s. A_{Ps} from synthetic (rectangle and diamond points) and observed data (grey circles and triangles) with Moho thickness $h = 0$ km and $h = 6$ km. Data belongs to sub-arrays I and III. (f) Theoretical curves of A_{PPp} as a function of A_{Ps} , with points indicating the Moho thickness ($h = 0, 5, 10, 15$ km). The grey points are extracted from observed data that is same as (c).

2005; Thybo & Artemieva, 2013). We demonstrate here that a gradual transition could jointly explain our observations of amplitudes for topside P-wave reflections from vertical autocorrelations and P-to-S transmissions on radial RFs. P-wave reflections and P-to-S transmissions have a different sensitivity to velocity gradients (e.g. Bostock, 1999; Tauzin et al., 2019). We illustrate this by plotting the transmission and reflection coefficients T_{ps} and R_{pp} as a function of the vertical extent h of a transitional layer adopting the contrasts in elastic properties for the Moho from Crust1.0 (Figure 10a). For this computation, we decompose the gradient in thin homogeneous layers and use a plane-wave matrix algorithm (Chapman, 2003; Ma et al., 2012; Tauzin et al., 2019). We use a reference frequency of 0.6 Hz, which is the center of the frequency band of analysis for long-period vertical RFs. We also show the coefficient dependence on various slowness.

581 Generally, the transmission coefficients Tps decrease smoothly from a sharp interface to
 582 a ~ 10 km-thick interface. In contrast, the reflection coefficients Rpp decrease abruptly
 583 and non-linearly with h from $\sim 10\%$ to 0% and reach at 0.6 Hz a minimum for a ~ 8
 584 km-thick layer. This means that a transitional layer tends to affect the reflectivity of P-wave
 585 reflections more than the reflectivity from direct P-to-S conversions (Bostock, 1999; Tauzin
 586 et al., 2019).

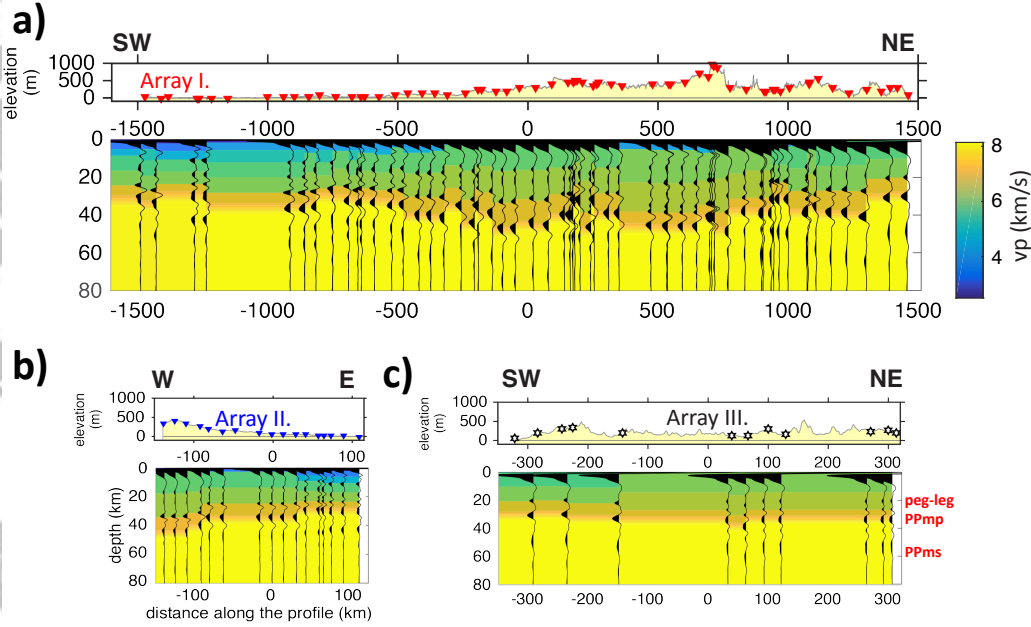


Figure 11. Superposition of synthetic P-wave auto-correlation signals (black traces) to the P-wave velocity structure (background colors) in the global crustal model Crust1.0 (Laske et al., 2013) modified using a transitional Moho layer 6 km thick.

587 When possible, we measured the amplitudes of the Moho conversions and reflections
 588 on the stacked observed vertical and radial waveforms for sub-arrays I and III from
 589 Figures 3 and 7. Those observations are shown in Figure 10b-d, e (grey) and f (grey). As
 590 shown by observation histograms in Figure 10b, the distribution of amplitude of the Moho
 591 reflection A_{PPp} has a maximum at 6% , whereas the amplitudes of conversion are more
 592 uniformly distributed over the range 0 - 15% . We observe a larger scatter in A_{Ps} than in
 593 A_{PPp} . These observations can be explained by the following: 1) the larger scatter in A_{Ps}
 594 can result from the effect of slowness variations, which is stronger on P-to-S conversions
 595 than on P-P reflections (Figure 10a); 2) the A_{Ps} scatters more in sub-array I (with SBs)
 596 than sub-array III (on a simple crust), possibly due to the effect of interferences from
 597 reverberations in shallow SB layers. Those effects can be simulated through wave-propagation
 598 in the Crust1.0 structure (Figures 10e, and 6, 12). The synthetic experiments confirm
 599 larger scatter in A_{Ps} for sub-array I, which spreads between $\sim 0\%$ to more than 10% , while
 600 the coefficients A_{PPp} fall within the ranges of 8 - 12% for a Moho width $h = 0$ km (black
 601 squares) and 2 - 6% for $h = 6$ km (blue squares). Meanwhile, results from sub-array III
 602 (red and magenta diamond points) have narrow distributions in A_{PPp} and A_{Ps} , possi-
 603 bly due to the exemption of contaminations by shallow SB layers. In conclusion, A_{PPp}
 604 offers more reliable constrains on the values of h . Therefore, from Figure 10f, we find that
 605 the solution explaining the amplitudes of the reflections is a transitional layer with a thick-
 606 ness slightly lower than 5 km. In Figure 11, we show the predicted waveforms for a 6 km-

607 thick gradient, from which we reported the measurements shown in Figure 10d. The pre-
608 dicted Moho amplitudes appear to be in better agreement with the observed data (Fig-
609 ure 4) than the predictions from a first-order discontinuity (Figure 6). We note that the
610 Moho transition can also be reduced to a value thinner than 5 km if we consider a com-
611 bination of possible mechanisms that can reduce the Moho reflection amplitudes, such
612 as crustal transmission losses, 3D scattering, and effects of inelastic attenuation. How-
613 ever, we would have to explain why such mechanisms do not similarly affect the
614 reflections from the top of the lower crust.

615 **6 Conclusion**

616 We investigated the efficiency of an autocorrelation technique to extract vertical
617 component receiver functions from teleseismic earthquake data and create images of the
618 crust beneath dense seismic arrays. Using synthetic and field-data examples, we com-
619 pared the performances of both vertical and radial RFs. We examined in particular the
620 contribution of reverberations in shallow sedimentary (SB) layers to the images formed
621 from both data types. Vertical RFs are simpler to interpret than radial RFs, although
622 they are not void of complexities associated with shallow reverberations. We show that
623 the operation of spectral whitening is critical for obtaining good quality images beneath
624 SBs, as it acts as a resonance removal filter. We processed broadband data from three
625 temporary USArray sub-arrays with quasi-linear geometry in the eastern US. By iden-
626 tifying pulses of reflected P-waves on the vertical autocorrelograms, we were able to iden-
627 tify the Moho and a laterally-variable crust structure beneath these subarrays. We ob-
628 served coherent signals along the three sub-arrays despite the presence of SBs. Compared
629 with the crustal model Crust1.0, our analysis suggests the existence of additional com-
630 plexity related to fine-scale layering and/or 3D structure. We developed a method to con-
631 strain the thickness of the Moho boundary from an amplitude analysis of reflected and
632 converted phases on vertical and radial component RFs. This analysis shows that the
633 Moho beneath eastern US is a transitional layer extending over a depth interval of up
634 to 5 km. The proposed method is highly complementary to other receiver-based meth-
635 ods and has the potential to advance our understanding of the crustal architecture with
636 or without SBs.

637 **Acknowledgments**

638 The IRIS Data Management Center was used for access to waveform data (available from
639 <http://service.iris.edu/fdsnws/dataselect/1/>). IRIS Data Services are funded through
640 the Seismological Facilities for the Advancement of Geoscience and EarthScope (SAGE)
641 Proposal of the National Science Foundation under Cooperative Agreement EAR-1261681.
642 We acknowledge Crust1.0 model (<https://igppweb.ucsd.edu/~gabi/crust1.html>).
643 We acknowledge the comments from reviewer Elmer Ruigrok, Associate Editor Sebastien
644 Chevrot, and an anonymous reviewer. B.T. has received funding from the European Union's
645 Horizon 2020 research and innovation program under the Marie Skłodowska-Curie grant
646 agreement No 793824.

647 **References**

- 648 Ahern, T., Casey, R., Barnes, D., Benson, R., & Knight, T. (2007). Seed standard
649 for the exchange of earthquake data reference manual format version 2.4. *In-*
650 *corporated Research Institutions for Seismology (IRIS)*, Seattle.
- 651 Ammon, C. (1991). The isolation of receiver effects from teleseismic P waveforms.
652 *Bull. Seismol. Soc. Am.*, *81*, 2504-2510.
- 653 Arndt, N. T., & Goldstein, S. L. (1989). An open boundary between lower continen-
654 tal crust and mantle: its role in crust formation and crustal recycling. *Tectono-*
655 *physics*, *161*(3-4), 201-212.

- 656 Becker, G., & Knapmeyer-Endrun, B. (2018). Crustal thickness across the trans-
 657 european suture zone from ambient noise autocorrelations. *Geophysical Journal*
 658 *International*, *212*(2), 1237–1254.
- 659 Bensen, G., Ritzwoller, M., Barmin, M., Levshin, A., Lin, F., Moschetti, M., ...
 660 Yang, Y. (2007). Processing seismic ambient noise data to obtain reliable
 661 broad-band surface wave dispersion measurements. *Geophysical Journal Inter-*
 662 *national*, *169*(3), 1239–1260.
- 663 Bostock, M. (1999). Seismic waves converted from velocity gradient anomalies in the
 664 Earth's upper mantle. *Geophys. J. Int.*, *138*, 747–756.
- 665 Buffoni, C., Schimmel, M., Sabbione, N. C., Rosa, M. L., & Connon, G. (2019).
 666 Crustal structure beneath tierra del fuego, argentina, inferred from seismic
 667 p-wave receiver functions and ambient noise autocorrelations. *Tectonophysics*,
 668 *751*, 41–53.
- 669 Burdick, & Helmberger. (1974). Time functions appropriate for deep earthquakes.
 670 *Bulletin of the Seismological Society of America*, *64*(5), 1419–1427.
- 671 Burdick, L. J., & Langston, C. A. (1977). Modeling crustal structure through the
 672 use of converted phases in teleseismic body-wave forms. *Bulletin of the Seismo-*
 673 *logical Society of America*, *67*(3), 677–691.
- 674 Chapman, C. (2003). Yet another elastic plane-wave, layer-matrix algorithm. *Geo-*
 675 *physical Journal International*, *154*(1), 212–223.
- 676 Claerbout, J. F. (1968). Synthesis of a layered medium from its acoustic transmis-
 677 sion response. *Geophysics*, *33*(2), 264–269.
- 678 Clayton, R. W., & Wiggins, R. A. (1976). Source shape estimation and deconvolu-
 679 tion of teleseismic bodywaves. *Geophysical Journal International*, *47*(1), 151–
 680 177.
- 681 Delph, J. R., Levander, A., & Niu, F. (2019). Constraining crustal properties using
 682 receiver functions and the autocorrelation of earthquake-generated body waves.
 683 *Journal of Geophysical Research: Solid Earth*.
- 684 Dufek, J., & Bergantz, G. (2005). Lower crustal magma genesis and preservation: a
 685 stochastic framework for the evaluation of basalt–crust interaction. *Journal of*
 686 *Petrology*, *46*(11), 2167–2195.
- 687 Efron, B., & Tibshirani, R. (1991). Statistical Data Analysis in the Computer Age.
 688 *Science*, *253*, 390–395.
- 689 Ekström, G., Nettles, M., & Dziewoński, A. (2012). The global cmt project 2004–
 690 2010: Centroid-moment tensors for 13,017 earthquakes. *Physics of the Earth*
 691 *and Planetary Interiors*, *200*, 1–9.
- 692 Frederiksen, A., & Delaney, C. (2015). Deriving crustal properties from the p coda
 693 without deconvolution: the southwestern superior province, north america.
 694 *Geophysical Journal International*, *201*(3), 1491–1506.
- 695 Furlong, K. P., & Fountain, D. M. (1986). Continental crustal underplating: Ther-
 696 mal considerations and seismic-petrologic consequences. *Journal of Geophysical*
 697 *Research: Solid Earth*, *91*(B8), 8285–8294.
- 698 Gorbatov, A., Saygin, E., & Kennett, B. (2013). Crustal properties from seismic sta-
 699 tion autocorrelograms. *Geophysical Journal International*, *192*(2), 861–870.
- 700 Helffrich, G. (2019, 02). Comment on "Crustal thickness across the Trans-
 701 European Suture Zone from ambient noise autocorrelations" by G. Becker
 702 and B. Knapmeyer-Endrun. *Geophysical Journal International*, *217*(2),
 703 906–908. Retrieved from <https://doi.org/10.1093/gji/ggz072> doi:
 704 10.1093/gji/ggz072
- 705 Kennett, B. (1983). *Seismic wave propagation in stratified media*. Cambridge, New
 706 York: Cambridge University Press.
- 707 Kennett, B. (2015). Lithosphere–asthenosphere p-wave reflectivity across australia.
 708 *Earth and Planetary Science Letters*, *431*, 225–235.
- 709 Kennett, B., & Engdahl, E. (1991). Travel times for global earthquake location and
 710 phase identification. *Geophys. J. Int.*, *105*, 429–465.

- 711 Kennett, B., & Furumura, T. (2016). Multiscale seismic heterogeneity in the conti-
712 nental lithosphere. *Geochemistry, Geophysics, Geosystems*, *17*(3), 791–809.
- 713 Kennett, B., & Saygin, E. (2015). The nature of the moho in australia from reflec-
714 tion profiling: A review. *GeoResJ*, *5*, 74–91.
- 715 Kennett, B., Saygin, E., & Salmon, M. (2015). Stacking autocorrelograms to map
716 moho depth with high spatial resolution in southeastern australia. *Geophysical
717 Research Letters*, *42*(18), 7490–7497.
- 718 King, P. B., & Beikman, H. M. (1974). *Geologic map of the united states*. USGS
719 Map Distribution.
- 720 Langston. (1979). Structure under mont Rainier, Washington, inferred from teleseis-
721 mic body waves. *J. Geophys. Res.*, *84*.
- 722 Langston. (2011). Wave-field continuation and decomposition for passive seismic
723 imaging under deep unconsolidated sediments. *Bulletin of the Seismological
724 Society of America*, *101*(5), 2176–2190.
- 725 Langston, C., & Hammer, J. (2001). The vertical component p-wave receiver func-
726 tion. *Bulletin of the Seismological Society of America*, *91*(6), 1805–1819.
- 727 Laske, G., Masters, G., Ma, Z., & Pasyanos, M. (2013). Update on crust1. 0-a 1-
728 degree global model of earth’s crust. In *Geophys. res. abstr* (Vol. 15, p. 2658).
- 729 Li, Niu, F., Yang, Y., & Tao, K. (2019). Joint inversion of rayleigh wave phase
730 velocity, particle motion, and teleseismic body wave data for sedimentary
731 structures. *Geophysical Research Letters*, *46*(12), 6469–6478.
- 732 Li, X.-Q., & Nábělek, J. L. (1999). Deconvolution of teleseismic body waves for
733 enhancing structure beneath a seismometer array. *Bulletin of the Seismological
734 Society of America*, *89*(1), 190–201.
- 735 Ma, Y., Wang, R., & Zhou, H. (2012). A note on the equivalence of three major
736 propagator algorithms for computational stability and efficiency. *Earthquake
737 Science*, *25*(1), 55–64.
- 738 Pham, T.-S., & Tkalčić, H. (2017). On the feasibility and use of teleseismic p wave
739 coda autocorrelation for mapping shallow seismic discontinuities. *Journal of
740 Geophysical Research: Solid Earth*, *122*, 3776–3791.
- 741 Pham, T.-S., & Tkalčić, H. (2018). Antarctic ice properties revealed from teleseismic
742 p-wave coda autocorrelation. *Journal of Geophysical Research: Solid Earth*.
- 743 Piana Agostinetti, N., Martini, F., & Mongan, J. (2018). Sedimentary basin in-
744 vestigation using receiver function: an east african rift case study. *Geophysical
745 Journal International*, *215*(3), 2105–2113.
- 746 Randall, G. (1989). Efficient calculation of differential seismograms for lithospheric
747 receiver functions. *Geophysical Journal International*, *99*(3), 469–481.
- 748 Romero, P., & Schimmel, M. (2018). Mapping the basement of the ebro basin in
749 spain with seismic ambient noise autocorrelations. *Journal of Geophysical Re-
750 search: Solid Earth*, *123*(6), 5052–5067.
- 751 Ruigrok, E., & Wapenaar, K. (2012). Global-phase seismic interferometry unveils p-
752 wave reflectivity below the himalayas and tibet. *Geophysical Research Letters*,
753 *39*(11).
- 754 Saygin, E., Cummins, P. R., & Lumley, D. (2017). Retrieval of the p wave reflec-
755 tivity response from autocorrelation of seismic noise: Jakarta basin, indonesia.
756 *Geophysical Research Letters*, *44*(2), 792–799.
- 757 Schimmel, M., & Paulssen, H. (1997). Noise reduction and detection of weak, coher-
758 ent signals through phase-weighted stacks. *Geophysical Journal International*,
759 *130*(2), 497–505.
- 760 Schruben, P. G., Arndt, R. E., & Bawiec, W. J. (1998). *Geology of the contermi-
761 nous united states at 1: 2,500,000 scale a digital representation of the 1974
762 pb king and hm beikman map* (No. 11). The Survey; For sale by USGS Map
763 Distribution,.
- 764 Schruben, P. G. A., Bawiec, R. E., King, W. J., Beikman, P. B., & Helen, M.
765 (1994). *Geology of the conterminous united states at 1: 2,500,000 scale—a*

- 766 digital representation of the 1974 pb king and hm beikman map.
- 767 Smith, W. H., & Sandwell, D. T. (1997). Global sea floor topography from satellite
- 768 altimetry and ship depth soundings. *Science*, *277*(5334), 1956–1962.
- 769 Sun, W., & Kennett, B. (2016). Receiver structure from teleseisms: Autocorrelation
- 770 and cross correlation. *Geophysical Research Letters*, *43*(12), 6234–6242.
- 771 Tao, K., Liu, T., Ning, J., & Niu, F. (2014). Estimating sedimentary and crustal
- 772 structure using wavefield continuation: theory, techniques and applications.
- 773 *Geophysical Journal International*, *197*(1), 443–457.
- 774 Tauzin, B., Pham, T.-S., & Tkalčić, H. (2019). Receiver functions from seismic inter-
- 775 ferometry: A practical guide. *Geophysical Journal International*, *217*, 1–24.
- 776 Taylor, G., Rost, S., & Houseman, G. (2016). Crustal imaging across the north ana-
- 777 tolian fault zone from the autocorrelation of ambient seismic noise. *Geophysical*
- 778 *Research Letters*, *43*(6), 2502–2509.
- 779 Thybo, H., & Artemieva, I. M. (2013). Moho and magmatic underplating in conti-
- 780 nental lithosphere. *Tectonophysics*, *609*, 605–619.
- 781 Tibuleac, I. M., & von Seggern, D. (2012). Crust-mantle boundary reflectors in
- 782 nevada from ambient seismic noise autocorrelations. *Geophysical Journal Inter-*
- 783 *national*, *189*(1), 493–500.
- 784 van IJsseldijk, J., Ruigrok, E., Verdel, A., & Weemstra, C. (2019). Shallow crustal
- 785 imaging using distant, high-magnitude earthquakes. *Geophysical Journal Inter-*
- 786 *national*.
- 787 Vinnik, L. (1977). Detection of waves converted from P to SV in the mantle. *Phys.*
- 788 *Earth Planet. Inter.*, *15*, 39–45.
- 789 Wapenaar, K., Draganov, D., Snieder, R., Campman, X., & Verdel, A. (2010). Tu-
- 790 torial on seismic interferometry: Part 1—basic principles and applications. *Geo-*
- 791 *physics*, *75*(5), 75A195–75A209.
- 792 White, R., & McKenzie, D. (1989). Magmatism at rift zones: the generation of vol-
- 793 canic continental margins and flood basalts. *Journal of Geophysical Research: Solid Earth*, *94*(B6), 7685–7729.
- 794
- 795 Yang, C., & Niu, F. (2019). Sedimentary structure of the western bohai bay basin
- 796 and other basins in north china revealed by frequency dependent p-wave parti-
- 797 cle motion. *Geodesy and Geodynamics*, *10*(5), 372–381.
- 798 Yu, Y., Song, J., Liu, K. H., & Gao, S. S. (2015). Determining crustal structure be-
- 799 neath seismic stations overlying a low-velocity sedimentary layer using receiver
- 800 functions. *Journal of Geophysical Research: Solid Earth*, *120*(5), 3208–3218.
- 801 Zheng, T., Zhao, L., & Chen, L. (2005). A detailed receiver function image of the
- 802 sedimentary structure in the bohai bay basin. *Physics of the Earth and Planetary*
- 803 *Interiors*, *152*(3), 129–143.